INTERNATIONAL JOURNAL FOR NUMERICAL METHODS IN FLUIDS
Int. J. Numer. Meth. Fluids 2013; **72**:895–911
Published online 14 January 2013 in Wiley Online Library (wileyonlinelibrary.com/journal/nmf). DOI: 10.1002/fld.3764

A lattice Boltzmann fictitious domain method for modeling red blood cell deformation and multiple-cell hydrodynamic interactions in flow

Xing Shi[1], Guang Lin[2,*,†], Jianfeng Zou[1] and Dmitry A. Fedosov[3]

[1]*School of Aeronautics and Aerospace, Zhejiang University, Hangzhou, 310027, P.R. China*
[2]*Pacific Northwest National Laboratory, 902 Battelle Blvd., P.O. Box 999, WA 99352, USA*
[3]*Institute of Complex Systems and Institute for Advanced Simulation, Forschungszentrum Jülich, Jülich, 52425, Germany*

SUMMARY

To model red blood cell (RBC) deformation and multiple-cell interactions in flow, the recently developed technique derived from the lattice Boltzmann method and the distributed Lagrange multiplier/fictitious domain method is extended to employ the mesoscopic network model for simulations of RBCs in flow. The flow is simulated by the lattice Boltzmann method with an external force, while the network model is used for modeling RBC deformation. The fluid–RBC interactions are enforced by the Lagrange multiplier. To validate parameters of the RBC network model, stretching tests on both coarse and fine meshes are performed and compared with the corresponding experimental data. Furthermore, RBC deformation in pipe and shear flows is simulated, revealing the capacity of the current method for modeling RBC deformation in various flows. Moreover, hydrodynamic interactions between two RBCs are studied in pipe flow. Numerical results illustrate that the leading cell always has a larger flow velocity and deformation, while the following cells move slower and deform less. Copyright © 2013 John Wiley & Sons, Ltd.

Received 26 June 2012; Revised 21 October 2012; Accepted 19 November 2012

KEY WORDS: erythrocyte; fictitious domain method; lattice Boltzmann method; fluid-structure interaction; parachute shape

1. INTRODUCTION

As the computational capacity of computers continues to increase, numerical simulations of red blood cells (RBC) attract increasing attention because of the important role of RBCs in blood circulation. Simulations of individual RBCs provide a down-to-cell approach to study blood flow. Pioneering and fundamental works conducted by Fung [1], Fung and Zweifach [2], Evans [3], Skalak and Branemark [4], and Secomb *et al*. [5], etc., explored the structure and properties of an RBC membrane and established mathematical RBC models. According to these studies, an RBC can be considered as a closed membrane filled with cytosol and immersed in plasma. The RBC has no nucleus, and both the cytosol and plasma are Newtonian fluids. The RBC membrane is composed of a phospholipid bilayer supported by a protein skeleton resistant to extension and compression. During the deformation in blood flow, RBCs roughly maintain their surface area and volume.

To represent the properties of an RBC membrane, there are two types of mathematical models at macroscopic and mesoscopic scales, respectively. The continuum description of an RBC is based on classic solid mechanics and has been widely used in the computation of RBC properties [1, 6], such as the equilibrium shape [6, 7], deformation in capillary flow [5], membrane motion in shear

*Correspondence to: Guang Lin, 902 Battelle Blvd., PO Box 999, MSIN K7-90, Richland, WA 99352.
†E-mail: Guang.Lin@pnl.gov

flow [8], and stretching by optical tweezers [9]. There are two types of mesoscopic RBC models described in literature. The first model represents an RBC as a soft body [10] using the discrete particle method. The second focuses on the membrane. Following the topology structure of an RBC cytoskeleton, Boey *et al*. [11] and Li *et al*. [12] constructed the membrane as a network of springs with proper constraints using coarse-grained molecular dynamics (CGMD). Pivkin and Karniadakis [13] and Fedosov *et al*. [14] proposed a coarse-graining rule, such that the spring network model representing the spectrin cytoskeleton of an RBC can be carried out with a coarse mesh to improve the computational efficiency. The spring network model at the spectrin level, where each spring corresponds to a single spectrin protein connection, becomes computationally demanding to simulate even several RBCs, while the coarse-grained RBC model allows simulations of several thousand RBCs. Furthermore, the mesoscopic techniques, such as dissipative particle dynamics [15], lattice Boltzmann method (LBM) [16], and multiparticle collision dynamics [17] are widely used in many other applications. In these algorithms, the network model of an RBC is natural and convenient to implement and to solve the fluid–structure interaction problems involving RBCs.

Another problem arising in fluid–RBC interactions is how to deal with the moving boundary. Pozrikidis [18] adopted the boundary integral method, which has certain difficulties in three-dimensional (3D) multiple-RBC simulations. In methods with fluid mesh, a straightforward strategy for the fluid–structure coupling is to treat the fluid–structure interface directly as the moving boundary on fluid mesh as with the conventional ALE method [19]. However, it may not be suitable for simulations with highly deformable RBCs. Because of an overly distorted fluid mesh, the remeshing procedure is always time consuming and difficult in complex topology [20]. Moreover, the algorithm is not robust enough for large solid deformations and complex geometries. An alternative is the so-called 'fixed-mesh method', which includes the immersed boundary (IB) method [21], immersed finite element method [22], and fictitious domain (FD) method [23]. These methods employ a similar treatment to deal with moving boundaries, where the fluid mesh is not altered because of the motion of solids, while coupling between the fluid and structure is performed through a pseudobody force. The fluid–structure coupling is carried out by an interpolation and distribution between the fluid and solid mesh without remeshing. Numerical simulations of RBC dynamics using IB and immersed finite element method are quite popular, where the structure motion explicitly follows the fluid velocity [24–26]. Recently, the fictitious domain method has been extended to fluid–elastic structure interaction problems [23, 27, 28] and to the interactions of cells and neutrally buoyant particles [29]. However, its application in modeling RBCs is limited in literature.

Our previous work involving the LBM distributed Lagrange multiplier/fictitious domain (DLM/FD) method [30] used the DLM/FD method with the lattice Boltzmann fluid solver. Although the anisotropic p-version high order finite element method was applied to simulate a thin structure [31], it was not suitable for modeling an RBC's very thin membrane. In this paper, we combine the LBM-DLM/FD method with the developed mesoscopic membrane model [14] for simulations of RBC deformation in several flows. The paper is organized as follows:

(1) Section 2 outlines mathematical formulation.
(2) In Section 3, three numerical tests including RBC stretching, RBC flowing through a cylindrical tube, and an RBC in shear flow are performed to validate the method.
(3) Section 4 presents conclusions.

2. MATHEMATICAL FORMULATION

2.1. Red blood cell model

A coarse-grained network model of the RBC membrane was first proposed by Boey *et al*. [11] and further developed by Li *et al*. [12], Pivkin and Karniadakis [13], and Fedosov *et al*. [14]. Here, we employ the RBC model by Fedosov *et al*. [14], where the membrane surface is triangulated with N nodes, E edges, and T triangles. The total energy of the system is defined as

$$V(\mathbf{x}_n) = V_{\text{in-plane}} + V_{\text{bending}} + V_{\text{surface}} + V_{\text{volume}}, \tag{1}$$

DOI: 10.1002/fld

where $\mathbf{x}_n$ represents the vertex coordinates and the in-plane energy is expressed by

$$V_{\text{in-plane}} = \sum_{\text{all edges}} V_{\text{wlc}} + \sum_{\text{all edges}} V_{\text{p}}. \tag{2}$$

Each edge in the network is a spring defined by two potentials—a wormlike chain with the energy V_{wlc} and a repulsive potential with the energy V_{p}, as follows:

$$V_{\text{wlc}} = \frac{k_{\text{B}} T l_{\max}}{4p} \frac{3x^2 - 2x^3}{1 - x}, \tag{3}$$

$$V_{\text{p}} = \begin{cases} -k_{\text{p}} \log l & m = 1 \\ \frac{k_{\text{p}}}{(m-1) l^{m-1}} & m > 1 \end{cases}, \tag{4}$$

where k_{B} is the Boltzmann constant; T is the temperature; l is the spring length; $l_{\max}$ is the maximum extension length of the spring; $x = l \,/\, l_{\max}$. p is the persistence length, k_{p} and m are the strength and power coefficients of the energy V_{p}, respectively.

The membrane-bending energy is given by:

$$V_{\text{bending}} = \sum_{\text{all triangle adjacents}} k_{\text{b}} \left[1 - \cos(\theta_{\alpha\beta} - \theta_0)\right], \tag{5}$$

where k_{b} is the bending coefficient and $\theta_{\alpha\beta}$ and θ_0 are the instantaneous and spontaneous angles between two adjacent triangles, respectively.

In Equation (1), the surface and volume terms are used to constrain the variation of the surface area and volume to be small and are presented as follows:

$$V_{\text{surface}} = \frac{k_{\text{s}} \left(S^{\text{total}} - S_0^{\text{total}}\right)^2}{2 S_0^{\text{total}}} + \sum_{\text{all triangles}} \frac{k_{\text{t}} \left(S - S_0\right)^2}{2 S_0} \tag{6}$$

$$V_{\text{volume}} = \frac{k_{\text{v}} (V - V_0)^2}{2 V_0}, \tag{7}$$

where S and V denote the surface area and volume, respectively. The subscript '0' denotes the desired value, while S and S^{total} correspond to the triangle area and the total membrane area, respectively. k_{s}, k_{t}, and k_{v} are the respective total surface area, local triangle area, and volume coefficients. Nodal forces are derived from the total energy as follows:

$$F_n^{\text{membrane}} = -\frac{\partial V(\mathbf{x}_n)}{\partial \mathbf{x}_n}. \tag{8}$$

2.2. Lattice Boltzman-distributed Lagrange multiplier/fictitious domain method

The developed LBM-DLM/FD method, based on a distributed Lagrange multiplier, is one of the fictitious domain methods within the lattice Boltzmann method framework for the goal of solving fluid–structure interaction problems. In this method, the fluid domain includes the union of the fluid and solid subdomains, while the Lagrange multiplier serves as the coupling term for the fluid and structure motions. The Lagrange multiplier's role can be considered as a type of body force that makes it possible to incorporate it in the external force term in lattice Boltzmann equations. The equations in the LBM-DLM/FD method include the fluid subdomain equations, the solid subdomain equations, and the equations constraining the fluid and solid motion.

The fluid flow is solved by the lattice Boltzmann method. The LBM is an Eulerian approach, which discretizes the continuous fluid particle velocity space into finite directions, $\mathbf{e}_i$. In the current paper, the 3D lattice with 15 velocities (D3Q15) is adopted. The corresponding directions $\mathbf{e}_i$ are defined as follows: $\mathbf{e}_0 = (0,0,0)$, $\mathbf{e}_{1,2} = (\pm 1,0,0)c$, $\mathbf{e}_{3,4} = (0,\pm 1,0)c$, $\mathbf{e}_{5,6} = (0,0,\pm 1)c$,

DOI: 10.1002/fld

$\mathbf{e}_{7,8} = (\pm 1, \pm 1, \pm 1)c$, $\mathbf{e}_{9,10} = (\mp 1, \pm 1, \pm 1)c$, $\mathbf{e}_{11,12} = (\mp 1, \mp 1, \pm 1)c$, $\mathbf{e}_{13,14} = (\pm 1, \mp 1, \pm 1)c$. The velocity scale c is defined as $c = \delta_x / \delta_t$, where δ_t and δ_x denote the time scale and lattice spacing, respectively. The form of lattice Boltzmann equations used here includes the distributed Lagrange multiplier, $\boldsymbol{\lambda}$, incorporated into the body force term under the incompressible limit [16, 30, 32, 33]

$$f_i(t + \delta_t, \mathbf{x} + \mathbf{e}_i \delta_t) = f_i(t, \mathbf{x}) - \frac{1}{\tau}\left(f_i - f_i^{\mathrm{eq}}\right) + \frac{w_i \delta_t}{c_{\mathrm{s}}^2}\left[\left(\boldsymbol{\lambda} + \rho_f \mathbf{f}_f\right) \cdot \mathbf{e}_i\right], \tag{9}$$

where f_i is the single-particle distribution function in the i-direction of the microscopic velocity, $\mathbf{f}_f$ is the external force acting on fluid, and w_i is the corresponding weighting factor of the density distribution in each velocity direction. τ is the relaxation time associated with the kinematic viscosity of a fluid and reflects the relaxation rate to the local equilibrium distribution f_i^{eq}, which can be evaluated as [16]

$$f_i^{\mathrm{eq}} = w_i \rho_f \left[1 + \frac{3}{c^2}(\mathbf{e}_i \cdot \mathbf{u}_f) + \frac{9}{2c^4}(\mathbf{e}_i \cdot \mathbf{u}_f)^2 - \frac{3}{2c^2}\mathbf{u}_f^2\right], \tag{10}$$

The pseudospeed of sound in a fluid is equal to $c_s = c / \sqrt{3}$ [16]. The macroscopic fluid velocity $\mathbf{u}_f$ and mass density ρ_f are obtained from the distribution functions as follows [16]:

$$\rho_f = \sum_i f_i, \quad \rho_f \mathbf{u}_f = \sum_i f_i \mathbf{e}_i. \tag{11}$$

The solid or structure motion is controlled by the following equation in a weak form [27]:

$$\int_{\Omega_s} ((\rho_s - \rho_f)\frac{\mathrm{d}\mathbf{u}_s}{\mathrm{d}t} - (\rho_s \mathbf{f}_s - \rho_f \mathbf{f}_f)) \cdot \boldsymbol{\varphi}_s \mathrm{d}\Omega_s - \int_{\Omega_s} [\nabla \cdot (\boldsymbol{\sigma}_s - \boldsymbol{\sigma}_f)] \cdot \boldsymbol{\varphi}_s \mathrm{d}\Omega_s + \int_{\Omega_s} \boldsymbol{\lambda} \cdot \boldsymbol{\varphi}_s \mathrm{d}\Omega_s = 0 \tag{12}$$

where $\mathbf{u}$ is the velocity, ρ is the mass density, $\mathbf{f}$ is the body force, and $\boldsymbol{\sigma}$ is the stress. The subscripts f and s correspond to the fluid and structure variables, respectively. $\boldsymbol{\varphi}_s$ is the weighting function.

We only consider the coupling between the motions of fluid and solid here

$$\int_{\Omega_s} (\mathbf{u}_s - \mathbf{u}_f) \cdot \boldsymbol{\gamma} \mathrm{d}\Omega_s = 0, \tag{13}$$

where $\boldsymbol{\gamma}$ is the corresponding weighting function. Often, RBC deformation in flow can be assumed to be a quasi-equilibrium process, which simplifies Equation (12) to a form without the acceleration term

$$\mathbf{F}(\mathbf{x}) = \int_{\Omega_s} (\rho_s \mathbf{f}_s - \rho_f \mathbf{f}_f) \cdot \boldsymbol{\varphi}_s \mathrm{d}\Omega_s + \int_{\Omega_s} [\nabla \cdot (\boldsymbol{\sigma}_s - \boldsymbol{\sigma}_f)] \cdot \boldsymbol{\varphi}_s \mathrm{d}\Omega_s - \int_{\Omega_s} \boldsymbol{\lambda} \cdot \boldsymbol{\varphi}_s \mathrm{d}\Omega_s = 0, \tag{14}$$

where the force term is the sum of the body, membrane, and fluid forces, and the pseudobody forces represented by the Lagrange multiplier. The whole system is decoupled to the fluid and solid subproblems using a fractional step scheme similar to that used in the DLM/FD method by Yu [27]. The fractional step scheme is expressed as follows:

(1) Assuming that f_i^n, $\boldsymbol{\lambda}^n$ at the time step n are given, we calculate f_i^* from Equation (9), omitting the collision operator. Then, we compute ρ_f^* and $\mathbf{u}_f^*$ from Equation (11). Here, the superscript '*' denotes an intermediate fractional step.

(2) The solid displacement in our method is computed from the force exerted on the solid. For this calculation we use an iterative method as follows:

(i) $\mathbf{x}^n \to \mathbf{x}^*$.

(ii) Calculate $\mathbf{F}(\mathbf{x}^*)$ in Equation (14) at the position $\mathbf{x}^*$.

(iii) If Equation (14) at the position $\mathbf{x}^*$ is not satisfied, update $\mathbf{x}^*$ by

$$\mathbf{x}^* + \varepsilon \mathbf{F}(\mathbf{x}^*) \to \mathbf{x}^*, \tag{15}$$

DOI: 10.1002/fld

where ε is a preselected small parameter that allows the iteration method to be stable and efficient. Then, go to step (ii).

(iv) If a termination criteria for Equation (14) is reached, $\mathbf{x}^* \to \mathbf{x}^{n+1}$.

(3) Using the first-order accurate scheme, we calculate the solid velocity as $\mathbf{u}_s^{n+1} = (\mathbf{x}^{n+1} - \mathbf{x}^n)/\delta_t$. In addition to the velocity constraint in Equation (13) and the fractional time scheme, we compute $\boldsymbol{\lambda}^{n+1}$ from the following equation:

$$\int_{\Omega_s} \boldsymbol{\lambda}^{n+1} \cdot \boldsymbol{\varphi}_s \mathrm{d}\Omega_s = \int_{\Omega_s} \boldsymbol{\lambda}^{n} \cdot \boldsymbol{\varphi}_s \mathrm{d}\Omega_s + \int_{\Omega_s} \rho_f^* \left(\frac{\mathbf{u}_s^{n+1} - \mathbf{u}_f^*}{\delta_t} \right) \cdot \boldsymbol{\varphi}_s \mathrm{d}\Omega_s, \tag{16}$$

where the fluid velocity at the RBC vertices is interpolated from the fluid mesh. If the collocation method is used, $\boldsymbol{\lambda}^{n+1}$ can be computed at each collocation point by

$$\boldsymbol{\lambda}^{n+1} = \boldsymbol{\lambda}^{n} + \rho_f^* \left(\frac{\mathbf{u}_s^{n+1} - \mathbf{u}_f^*}{\delta_t} \right). \tag{17}$$

(4) We distribute λ from the RBC network to the fluid grid as follows:

$$\boldsymbol{\lambda}_f = \int_{\Omega_s} \boldsymbol{\lambda} \delta(\mathbf{x}_f - \mathbf{x}_s) \mathrm{d}\Omega_s, \tag{18}$$

where the numerical $\delta(\mathbf{x})$ function is approximated as

$$\delta(\mathbf{x}) = d_h(x) \cdot d_h(y) \cdot d_h(z) \tag{19}$$

and

$$d_h(r) = \begin{cases} \frac{1}{8h} \left(3 - 2\frac{|r|}{h} + \sqrt{1 + 4\frac{|r|}{h} - 4\left(\frac{|r|}{h}\right)^2} \right) & |r| < h \\ \frac{1}{8h} \left(5 - 2\frac{|r|}{h} - \sqrt{-7 + 12\frac{|r|}{h} - 4\left(\frac{|r|}{h}\right)^2} \right) & h \leqslant |r| < 2h \\ 0 & \text{otherwise} \end{cases} \tag{20}$$

in LBM, where $h = \delta_x$.

(5) We calculate the intermediate distribution function f_i^{**} as follows:

$$f_i^{**} = f_i^* + \frac{w_i \delta_t}{c_s^2} \left[\left(\boldsymbol{\lambda}_f^{n+1} - \boldsymbol{\lambda}_f^{n} \right) \cdot \mathbf{e}_i \right]. \tag{21}$$

(6) We compute the distribution function f_i^{n+1} at the time step $n + 1$ as

$$f_i^{n+1} = f_i^{**} - \frac{1}{\tau} \left(f_i^{**} - f_i^{eq**} \right). \tag{22}$$

In contrast to the IB method where the displacement is computed directly using the interpolated velocity of the fluid field, the preceding steps correspond to the implicit calculation of the displacement of the solid part. This appears to be very robust and accurate, because the implicit calculation of the displacement of a solid is more stable, while the IB method may be too stiff especially for large solid deformations.

DOI: 10.1002/fld

3. NUMERICAL SIMULATIONS AND VALIDATION

3.1. Stretching test

RBC stretching experiments using optical tweezers [9, 34] have been performed to obtain the RBC elastic properties. Figure 1 shows a schematic of RBC stretching with a pair of forces applied in opposite directions, where the longitudinal and transverse diameters are measured. The RBC model is validated using the membrane parameters of the previous work [14] with the shear and bending moduli of the RBC set to 6.3 μN/m and $2.4 \times 10^{-19}\mathrm{N} \cdot \mathrm{m}$, respectively. The stretching force is imposed on 2% of the total membrane vertices at the RBC sides (shown in Figure 1). Two networks, coarse with 500 nodes and fine with 3000 nodes, are considered.

In Figure 2, the simulated longitudinal and transverse diameters for the coarse and fine networks are almost identical and compare well with the experimental data [9] and the numerical results [12, 14]. A disagreement in the transverse diameter may be partially due to experimental errors arising from the fact that the optical measurements were performed from a single observation angle. RBCs subjected to stretching may rotate around the stretching direction, and therefore

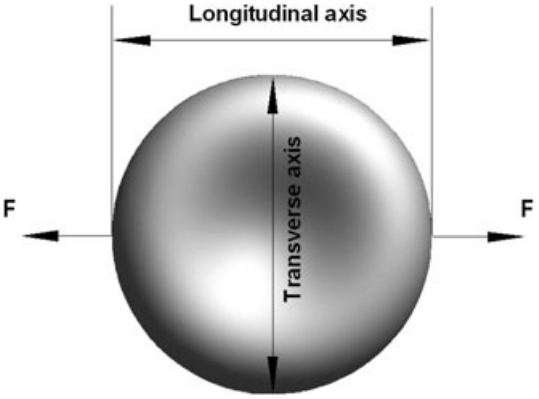

Figure 1. Schematic of RBC stretching.

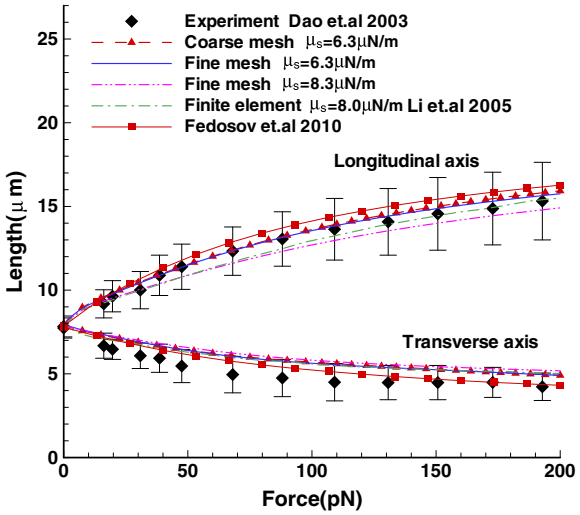

Figure 2. Longitudinal and transverse diameter variations under load. Experimental data are adopted from Dao *et al*. [9].

DOI: 10.1002/fld

coarse mesh fine mesh CGMD

Figure 3. Comparison of RBC deformation at a stretching force of 85 pN.

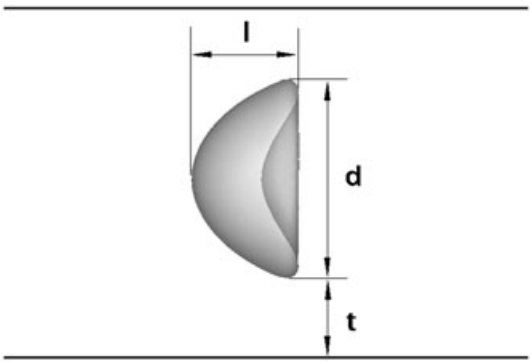

Figure 4. Schematic of the deformation index.

measurements from a single observation angle may result in underprediction of the maximum transverse diameter. However, the simulation results remain within the experimental error bars. Figure 3 shows the comparison of membrane deformation between the current method and the previous CGMD simulations [12] at a stretching force of 85 pN. The results from both approaches are similar and support the conclusion that 500 nodes to represent the RBC membrane are accurate enough.

3.2. Red blood cells in tube flow

Red blood cells flowing in a cylindrical tube are a basic model for blood flow in microvessels. The behavior of RBCs in flow, such as deformation, migration, and aggregation, greatly affects blood flow. The main function of RBCs is the release of oxygen, where the cell deformability is important for normal blood flow in microcirculation. The deformation of RBCs in response to an external force is usually measured by the deformation index (DI) defined as [35]

$$DI = \frac{l}{d}. \tag{23}$$

As shown in Figure 4, l and d are the length and diameter of an RBC, respectively, and t denotes the thickness of the RBC free layer. The deformation of an RBC is related to the external force exerted by the fluid and the elastic resistance of the cell membrane characterized by a capillary number (Ca) expressed as

$$Ca = \frac{U_{\mathrm{m}}\mu_{\mathrm{f}}}{\mu_{\mathrm{s}}}, \tag{24}$$

where U_{m} is the mean flow velocity, μ_{f} is the fluid viscosity, and μ_{s} is the membrane shear modulus.

DOI: 10.1002/fld

Pozrikidis [18] and Zhao *et al*. [36] simulated RBCs flowing through a narrow cylindrical tube using the boundary integral method. For comparison and validation, we employed the same geometry configuration used in [18] and [36]. The diameter of the tube is equal to 9.02 μm, corresponding to 78 lattice units. The periodic boundary conditions are imposed at the inlet and outlet, resulting in cells separated by the distance of $2a$, where a is defined as

$$a = (3V / 4\pi)^{\frac{1}{3}}, \tag{25}$$

where V is the volume of the cell. According to Fung's experimental data [1], the average volume of a healthy RBC is about 93 μm^3, and therefore we find that $a = 2.82$ μm. A constant body force is applied to drive the flow.

Figure 5 illustrates RBC shapes at different *Ca* numbers after the steady state is reached. The corresponding average thicknesses of the RBC free layer are 0.79, 0.96, and 1.13 μm, respectively. The cell moves along the flow axis with a constant velocity and the shape of an RBC changes from biconcave to parachute shape in tube flow. The transition to parachute shape is known to lower the flow resistance [14]. The *DI–Ca* relationship is shown in Figure 6(a) and indicates the increase of *DI* as the *Ca* number increases. The *DI–Ca* relationship is clearly nonlinear and was fitted with an exponential function in experiments of Tsukada *et al*. [35]. The *DI–Ca* correlation also reveals that RBC deformation in microtubes may be favorable for oxygen delivery. At high *Ca* numbers, RBCs elongate along the flow, resulting in a larger surface area next to the endothelium that potentially facilitates better oxygen delivery.

To compare with the experiment of Tsukada *et al*. [35], we also perform the simulation of an RBC in a tube with the diameter of 9.3 μm shown in Figure 6(b). On the basis of the physiological parameters $\mu_f = 1.2$cP and $\mu_s = 5.1$ μN/m, the *Ca* numbers that correspond to the range of RBC velocities between 1 and 4 mm/s studied in experiments [35] are in the range of 0.235∼0.941. In comparison with the previous simulations [36] and experiments [35] Figures 5 and 6 show that the predictions of RBC deformation by the present computational method are similar to those obtained by other numerical methods and experimentally.

Another important observation made in tube flow is the Fåhræus effect. We define the tube hematocrit, HCT_T, as the RBC volume fraction and the discharge hematocrit, HCT_D, as the ratio of the volumetric flow rate of RBCs per unit time to the total flow rate of the suspension. Then, the ratio between HCT_T and HCT_D can be expressed similar to that by Pozrikidis [18], as follows:

$$\frac{HCT_T}{HCT_D} = \frac{U_m}{U_c}, \tag{26}$$

where U_m is the mean flow velocity and U_c is the translational RBC velocity. The Fåhræus effect predicts this ratio to be lower than unity, which means that the RBC travels faster than the mean flow.

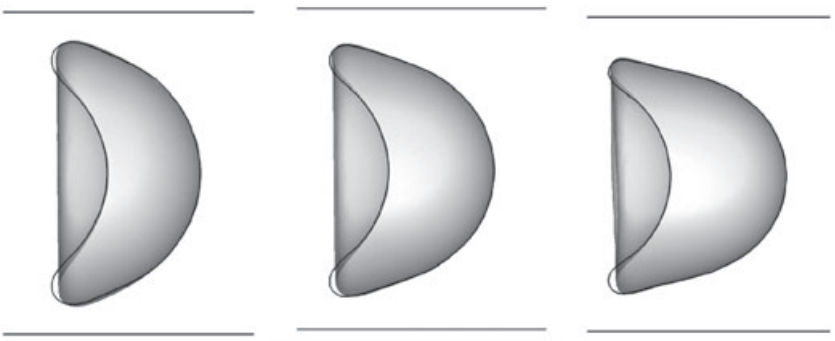

Ca=0.0502 *Ca*=0.105 *Ca*=0.215

Figure 5. Shapes of RBCs at different *Ca* numbers obtained with the LBM-DLM/FD method. The solid lines show the results by Zhao *et al*. [36], where the corresponding *Ca* numbers are 0.05, 0.101, and 0.203, respectively.

DOI: 10.1002/fld

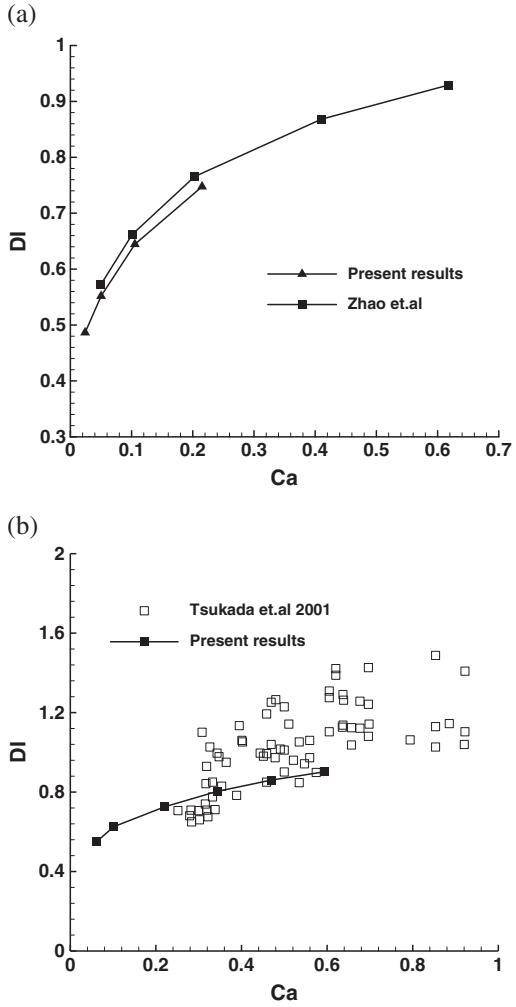

Figure 6. Deformation index (*DI*) for various *Ca* numbers. (a) Comparison with numerical results [36] and (b) comparison with experimental data [35].

Figure 7 shows that the simulation results are able to correctly capture the Fåhræus effect and they agree with the numerical results of Pozrikidis [18]. As the *Ca* number increases, the fluid layer between the RBC and the capillary wall becomes thicker (see Figure 5), which results in the RBC to attain a higher velocity and leads to the decrease of the ratio $HCT_{\mathrm{T}}/HCT_{\mathrm{D}}$.

There are several constraints for fluid–RBC interactions in the LBM-DLM/FD method that may affect numerical stability. The characteristic length scale L_{s} of a membrane network must meet the requirement of $\delta_{\mathrm{x}} \leqslant L_{\mathrm{s}}$ (see Ref. [37] for details). Moreover, the approximation of the δ function in Equation (19), which indicates that the radius of the influence domain for each membrane node is $2\delta_{\mathrm{x}}$, results in the lower bound for δ_{x} to be $L_{\mathrm{s}}/\left(2\sqrt{3}\right)$. If L_{s} exceeds this limit, the influence domain of each membrane node cannot cover all fluid grid points affected by the solid, which would require another interpolation algorithm. We performed a simulation test in close proximity to the lower limit for the tube of the diameter 9.3 μm. The RBC network uses 500 nodes, the flow parameters are kept the same except for the lattice spacing, and δ_x is varied between $0.26L_{\mathrm{s}} \sim 0.65L_{\mathrm{s}}$. The characteristic length of an edge is computed as the average of all network edges and is equal to approximately 0.55 μm. Figure 8 presents the pressure distribution near the RBC after reaching a steady state. We found that a pressure oscillation occurs near the interface and becomes larger as δ_{x} decreases. This pressure oscillation may cause numerical instability. Note that the pressure oscillation already

DOI: 10.1002/fld

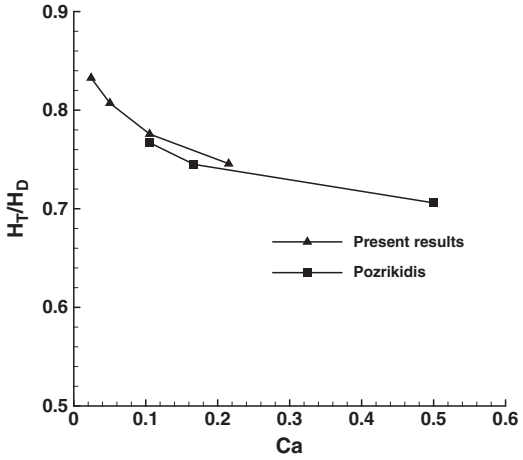

Figure 7. Ratio of the tube to the discharge hematocrit with respect to the *Ca* number.

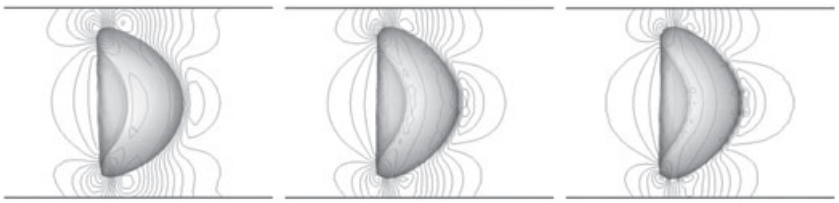

Figure 8. The pressure distribution in the middle cut plane.

appears as δ_x decreases to $L_s / 3$ because the network edges are not strictly equal to L_s. Therefore, the recommended mesh size constraint should be $0.5L_s < \delta_x < L_s$. Also, for strong membrane deformations, a large ratio of triangle edges may exist and could require a remeshing strategy of the membrane network.

3.3. Red blood cells in shear flow

A number of investigations of RBC motion in shear flow have been performed. Two characteristic types of RBC dynamics, tumbling and tank-treading motion, are reported [38, 39]. Several nondimensional numbers may control RBC dynamics in shear flow: the viscosity ratio between the cytoplasm and the surrounding fluid, $\mu^* = \mu_{in}/\mu_{out}$ and the capillary number defined as

$$Ca = \frac{\dot{\gamma} a \mu_{out}}{\mu_s}, \tag{27}$$

where $\dot{\gamma}$ is the shear rate, μ_{in} and μ_{out} are the viscosity of the cytoplasm and of the surrounding fluid, while μ_s is the shear modulus of the RBC membrane. The capillary number characterizes the ratio of the shear stress applied by the surrounding fluid to the elastic resistance of the RBC membrane. The following simulations focus on the effect of the capillary number on the RBC dynamics in shear flow with unit viscosity ratio.

The simulation setup is shown in Figure 9, where the cell is placed in the center of the computational domain. The shear plane is parallel to the $x - y$ plane. Two parallel walls moving in opposite directions are used to generate the linear shear flow. The boundaries in x and z directions are set to be periodic. The resolution in the computational domain is $60 \times 60 \times 60$. The RBC membrane consists of 500 nodes and 996 triangle elements. The Reynolds number is kept below 0.1.

DOI: 10.1002/fld

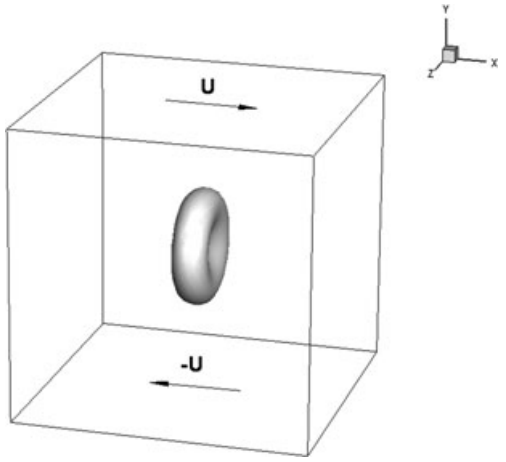

Figure 9. Schematic of a RBC in shear flow.

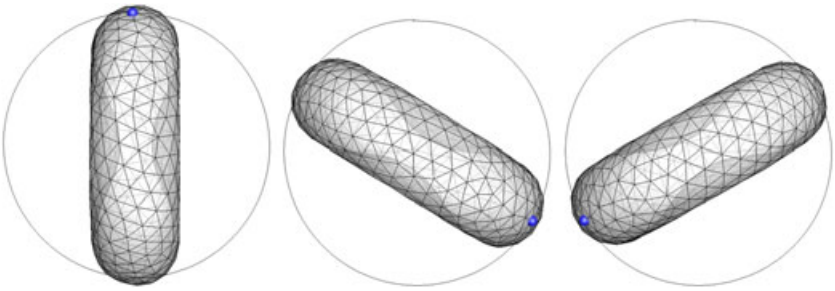

Figure 10. RBC tumbling at different times within the period of full rotation, $Ca = 0.001$.

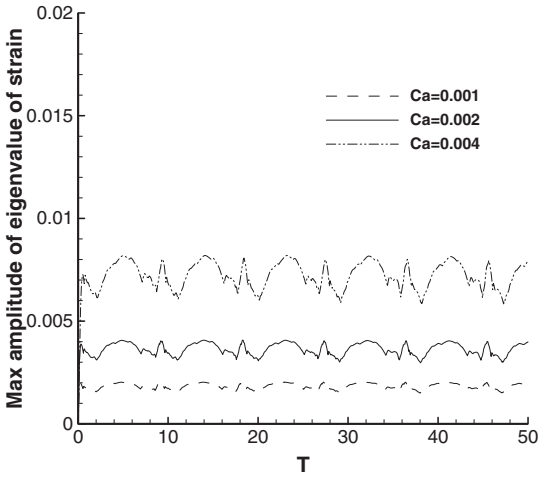

Figure 11. Temporal evolution of the maximum eigenvalue of the Green's strain at different *Ca* numbers (T denotes time normalized by $\dot{\gamma}$).

Tumbling occurs at low *Ca* numbers, indicating that the elastic forces in the membrane are able to resist deformation caused by shear stresses exerted by the flow. Figure 10 shows the typical tumbling motion at $Ca = 0.001$. A marker is placed on the membrane to track the membrane motion. The drawn circle is the trajectory of the marker over the period of one rotation. As illustrated in Figure 10, the RBC rotates as a rigid body with no visible membrane deformation. An asymmetric

DOI: 10.1002/fld

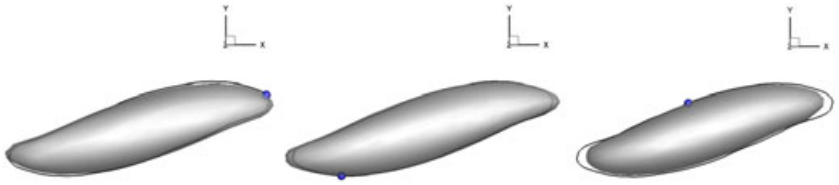

Figure 12. Elongated tank-treading RBC at various times within a period, $Ca = 1.45$.

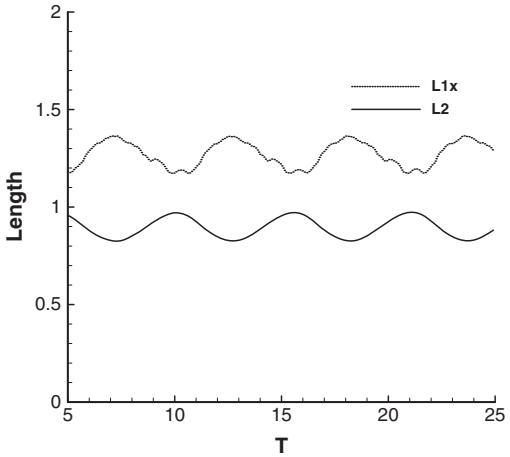

Figure 13. Temporal evolution of the RBC length and width (T denotes time normalized by $\dot{\gamma}$).

network structure may cause an asymmetric flow motion so that the trajectory of the marker may not be fully in the z-plane. For further quantitative analysis we define the deformation gradient as follows:

$$\mathbf{F} = \frac{\partial \mathbf{x}}{\partial \mathbf{X}}, \tag{28}$$

where $\mathbf{x}$ is the current configuration, and $\mathbf{X}$ is the initial structure of the membrane. We use the Green's strain tensor to measure the deformation, which is defined as

$$\mathbf{E} = \frac{1}{2}(\mathbf{F}^{\mathbf{T}} \cdot \mathbf{F} - \mathbf{I}) \tag{29}$$

Figure 11 shows the temporal evolution of the maximum principal strain and confirms that the deformation of an RBC membrane is small. However, the strain becomes larger as the Ca number increases.

Red blood cell motion transfers to the tank-treading dynamics when the stress exerted by the fluid exceeds a certain value to overcome intramembrane elastic forces. Figure 12 illustrates how the position of the membrane material marker moves around the cell, indicating that the trajectory is no longer a circle but has an ellipsoidal-like shape. Note that in Figure 12 we removed the rigid translational displacement of the center of mass to characterize the essential RBC deformation. We found that the trajectory of the marker is the same for every tank-treading period, while the RBC shape varies. Figure 13 presents the periodic variation of the RBC width in the z direction (L2) and of the elongated cell length (L1x) projected on the x axis, where both are normalized by the RBC diameter in equilibrium. Such variations of the shape deformation are called 'breathing' phenomena [38].

The early experiments [40] found that the RBC tank-treading frequency is independent of a suspending fluid. Tran-Son-Tay *et al*. [41] later reported that the dependence is almost linear with respect to the shear rate and the slope of the frequency-shear rate curve is equal to about 0.22 for young RBCs and to approximately 0.18 for old RBCs. Figure 14 shows the tank-treading frequency

DOI: 10.1002/fld

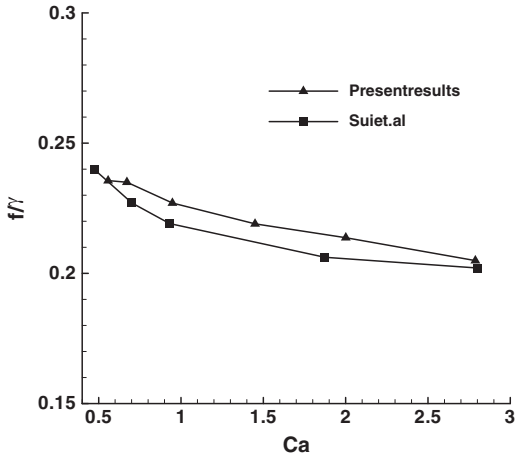

Figure 14. Nondimensional tank-treading frequency at different *Ca* numbers.

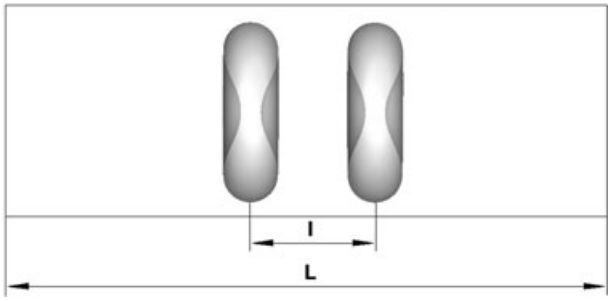

Figure 15. Schematic of the simulation setup for hydrodynamic coupling between two cells.

nondimensionalized by the shear rate versus the *Ca* number. Simulated tank-treading frequencies decrease slightly with the increase of the *Ca* number. This trend agrees with the computations of Sui *et al*. [39]. Although the nondimensional tank-treading frequency is not a constant, its variation is small and is close to the experimental values of Tran-Son-Tay *et al*. [41].

3.4. Hydrodynamic interactions between two cells

Next we show the capacity of the proposed method in simulating multiple cells. The simulation configuration is shown in Figure 15, where two cells are placed in the tube. The flow direction is from left to right. For convenience, we define the leading cell, the right one, as Cell 1 and the other as Cell 2. The length of the tube is $L = 11.7a$. The centroids of the cells are placed on the tube axis, while the distance between the cell centroids is defined as l. The volume fraction of RBCs in the tube is 8.3%. The diameter of the tube is 9.3 μm and occupies 68 lattices. The pressure drop is set to 0.8. The periodic boundary conditions are imposed at both inlet and outlet and the RBCs are placed at a distance $l = L/6$ (about $1.95a$).

Figure 16 presents the evolution of relative velocity and of the translational velocities scaled by the terminal velocity of the cells, U_{T}. The relative velocity is defined as

$$U_{\mathrm{rel}} = \frac{U_2 - U_1}{U_{\mathrm{T}}}\,, \tag{30}$$

where U_1 and U_2 are the translational velocities of Cell 1 and Cell 2, respectively. The distance between the centroids of RBCs is plotted in Figure 17. It is clear that Cell 1 moves faster than Cell 2. As the distance between the cells increases, the translational velocities of the RBCs tend to become identical. However, the evolution of cell velocities is different. The velocity of Cell 2 increases

DOI: 10.1002/fld

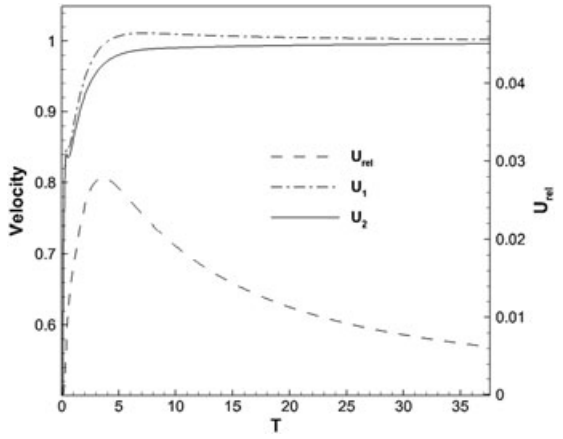

Figure 16. Translational and relative velocities of RBCs during hydrodynamic coupling between two cells.

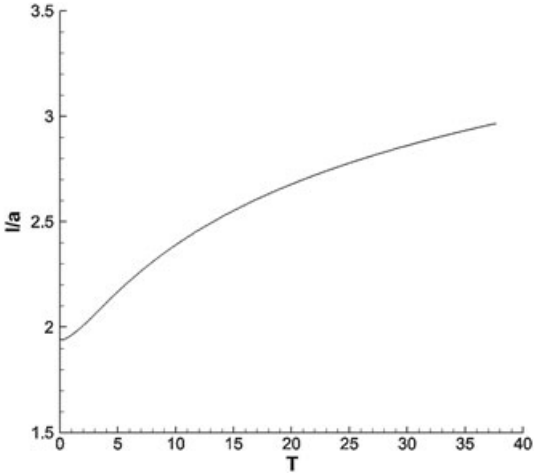

Figure 17. Distance between the centroids of the two interacting RBCs.

monotonically with time. The velocity of Cell 1 increases rapidly to the maximum value, which is even greater than U_{T}, and then decreases asymptotically to U_{T}. The distance l keeps increasing, which indicates that the hydrodynamic interaction range between the cells expands, however, the intensity of the hydrodynamic interactions decreases. As indicated by Pozrikidis [18], when $l > 3.5a$, the hydrodynamic interactions are weak, and can be ignored.

Figure 18 plots the deformation index versus time, while Figure 19 shows several snapshots at different times. We can see that the *DI*–time relation is similar to the velocity–time relation in Figure 16, which implies that the deformation depends on the translational velocity. The deformation of Cell 1 is stronger than that of Cell 2 at all times, but the difference in the *DI* number decreases with time. The difference in cell shapes can be also seen in Figure 19. At the initial stage, the curvature in the front part of Cell 1 is smaller than that of Cell 2. As the cells separate and their interaction becomes weak, the front part of Cell 1 becomes 'blunt', while that of Cell 2 becomes 'sharp'. Finally, the shapes of Cell 1 and Cell 2 become similar and approach a steady shape.

We can conclude that at the beginning the RBCs repel each other and the hydrodynamic interactions are weakened. The leading cell has always a larger translational velocity and deformation, while the following cell moves slower and deforms less. The motion of the cells tends to reduce the difference between them both in shape and velocity.

DOI: 10.1002/fld

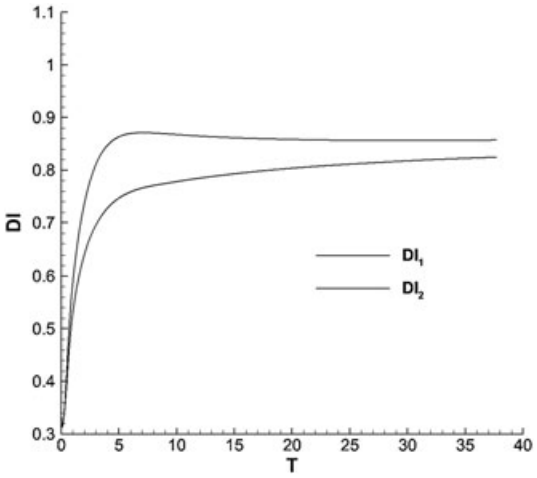

Figure 18. *DI*–time relationship of the two interacting RBCs.

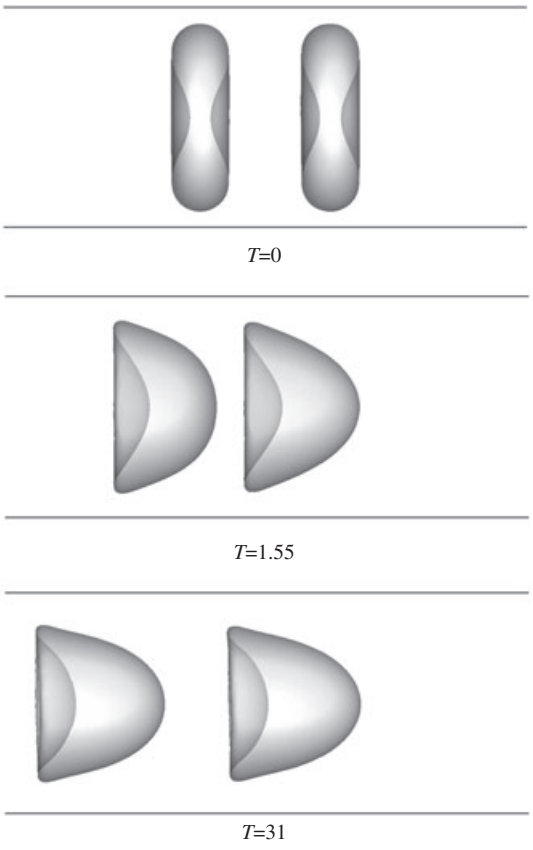

Figure 19. Snapshots of the shapes of the two interacting RBCs at different times.

4. CONCLUSIONS

The accurate prediction of RBC deformation in flow poses a new challenge in numerical methods for modeling flow–structure interactions. Such methods can be used in many applications including the investigation of normal blood flow in microcirculation and of blood flow in various diseases such as deep venous thrombosis, atherosclerosis, acquired immunodeficiency syndrome (AIDS),

DOI: 10.1002/fld

myeloma, etc. [42–44]. Additionally, the accurate modeling of cells and capsules in flow has a variety of engineering and material science applications.

In this paper, we extended the recently developed LBM-DLM/FD method to simulate RBC deformation in various flows. The developed mesoscopic model of an RBC membrane was successfully coupled with the LBM-DLM/FD algorithm. Two classical tests, RBCs flowing in a capillary tube and in shear flow, were used to validate the presented method. The simulation results are consistent with the previous numerical and experimental work, which confirms that the presented algorithm is suitable for the investigation of flow behavior of RBCs. Finally, hydrodynamic interactions between two RBCs were also studied illustrating the coupling between the cell velocities and deformation in flow.

ACKNOWLEDGEMENTS

Xing Shi and Jianfeng Zou would like to acknowledge support from the National Natural Science Foundation of China (Grant No. 10902098) and the Fundamental Research Funds of the Central Universities (Program No. 2010QNA40107). Guang Lin also acknowledges support from the U.S. Department of Energy (DOE) Office of Science's Advanced Scientific Computing Research Applied Mathematics program. Dmitry A. Fedosov acknowledges funding by the Alexander von Humboldt Foundation. A portion of the computations were performed using PNNL Institutional Computing cluster systems, and computational resources from the National Energy Research Scientific Computing Center at Lawrence Berkeley National Laboratory. PNNL is operated by Battelle for the DOE under Contract DE-AC05-76RL01830.

REFERENCES

1. Fung YC. *Biomechanics: Mechanical Properties of Living Tissues*, (2nd edn). Springer-Verlag: New York, 1993.
2. Fung YC, Zweifach BW. Microcirculation: Mechanics of blood low in capillaries. *Annual Review of Fluid Mechanics* 1971; **3**:189–210.
3. Evans EA. New membrane concept applied to the analysis of fluid shear- and micropipette-deformed red blood cells. *Biophysical Journal* 1973; **13**:941–954.
4. Skalak R, Branemark PI. Deformation of red blood cells in capillaries. *Science* 1969; **164**:717–719.
5. Secomb TW, Skalak R, Özkaya N, Gross JF. Flow of axisymmetric red blood cells in narrow capillaries. *Journal of Fluid Mechanics* 1986; **163**:405–423.
6. Zarda PR, Chien S, Skalak R. Elastic deformations of red blood cells. *Journal of Biomechanics* 1977; **10**:211–221.
7. McMillan DE, Mitchell TP, Utterback NG. Deformational strain energy and erythrocyte shape. *Journal of Biomechanics* 1986; **19**:275–286.
8. Eggleton CD, Popel AS. Large deformation of red blood cell ghosts in a simple shear flow. *Physics of Fluids* 1998; **10**:1834–1845.
9. Dao M, Lim CT, Suresh S. Mechanics of the human red blood cell deformed by optical tweezers. *Journal of the Mechanics and Physics of Solids* 2003; **51**:2259–2280.
10. Boryczko K, Dzwinel W, Yuen DA. Dynamical clustering of red blood cells in capillary vessels. *Journal of Molecular Modeling* 2003; **9**:16–33.
11. Boey SK, Boal DH, Discher DE. Simulations of the erythrocyte cytoskeleton at large deformation. I. Microscopic models. *Biophysical Journal* 1998; **75**:1573–1583.
12. Li J, Dao M, Lim CT, Suresh S. Spectrin-level modeling of the cytoskeleton and optical tweezers stretching of the erythrocyte. *Biophysical Journal* 2005; **88**:3707–3719.
13. Pivkin IV, Karniadakis GE. Accurate coarse-grained modeling of red blood cells. *Physical Review Letters* 2008; **101**:118105.
14. Fedosov DA, Caswell B, Karniadakis GE. A multiscale red blood cell model with accurate mechanics, rheology, and dynamics. *Biophysical Journal* 2010; **98**:2215–2225.
15. Groot RD, Warren PB. Dissipative particle dynamics: Bridging the gap between atomistic and mesoscopic simulation. *Journal of Chemical Physics* 1997; **107**:4423–4435.
16. Chen S, Doolen GD. Lattice Boltzmann method for fluid flows. *Annual Review of Fluid Mechanics* 1998; **30**:329–364.
17. Malevanets A, Kapral R. Mesoscopic model for solvent dynamics. *Journal of Chemical Physics* 1999; **110**:8605–8613.
18. Pozrikidis C. Axisymmetric motion of a file of red blood cells through capillaries. *Physics of Fluids* 2005; **17**:031503.
19. Donea J, Giuliani S, Halleux JP. An arbitrary Lagrangian–Eulerian finite element method for transient dynamic fluid–structure interactions. *Computer Methods in Applied Mechanics and Engineering* 1982; **33**:689–723.
20. De Hart J, Peters GWM, Schreurs PJG, Baaijens FPT. A three-dimensional computational analysis of fluid–structure interaction in the aortic valve. *Journal of Biomechanics* 2003; **36**:103–112.
21. Peskin CS. Numerical analysis of blood flow in the heart. *Journal of Computational Physics* 1977; **25**:220–252.

DOI: 10.1002/fld

22. Zhang L, Gerstenberger A, Wang X, Liu WK. Immersed finite element method. *Computer Methods in Applied Mechanics and Engineering* 2004; **193**:2051–2067.
23. Glowinski R, Pan TW, Périaux J. A fictitious domain method for external incompressible viscous flow modeled by Navier-Stokes equations. *Computer Methods in Applied Mechanics and Engineering* 1994; **112**:133–148.
24. Liu Y, Liu WK. Rheology of red blood cell aggregation by computer simulation. *Journal of Computational Physics* 2006; **220**:139–154.
25. Dupin MM, Halliday I, Care CM, Munn LL. Lattice Boltzmann modelling of blood cell dynamics. *International Journal of Computational Fluid Dynamics* 2008; **22**:481–492.
26. Zhang J, Johnson PC, Popel AS. Red blood cell aggregation and dissociation in shear flows simulated by lattice Boltzmann method. *Journal of Biomechanics* 2008; **41**:47–55.
27. Yu Z. A DLM/FD method for fluid/flexible-body interactions. *Journal of Computational Physics* 2005; **207**:1–27.
28. Baaijens FPT. A fictitious domain/mortar element method for fluid-structure interaction. *International Journal of Numerical Methods in Fluids* 2001; **35**:743–761.
29. Pan TW, Shi L, Glowinski R. A DLM/FD/IB method for simulating cell/cell and cell/particle interaction in microchannels. *Chinese Annals of Mathematics - Series B* 2010; **31**:975–990.
30. Shi X, Lim SP. A LBM-DLM/FD method for 3D fluid-structure interactions. *Journal of Computational Physics* 2007; **226**:2028–2043.
31. Düster A, Bröker H, Rank E. The p-version of the finite element method for three-dimensional curved thin walled structures. *International Journal for Numerical Methods in Engineering* 2001; **52**:673–703.
32. Nourgaliev RR, Dinh TN, Theofanous TG, Joseph D. The lattice Boltzmann equation method: theoretical interpretation, numerics and implications. *International Journal of Multiphase Flow* 2003; **29**:117–169.
33. Lee T, Lin CL. Pressure evolution lattice-Boltzmann-equation method for two-phase flow with phase change. *Physical Review E* 2003; **67**:056703.
34. Mills JP, Qie L, Dao M, Lim CT, Suresh S. Nonlinear elastic and viscoelastic deformation of the human red blood cell with optical tweezers. *Mechanics and Chemistry of Biosystems* 2004; **1**:169–180.
35. Tsukada K, Sekizuka E, Oshio C, Minamitani H. Direct measurement of erythrocyte deformability in diabetes mellitus with transparent microchannel capillary model and high-speed video camera system. *Microvascular Research* 2001; **61**:231–239.
36. Zhao H, Isfahani AHG, Olson LN, Freund JB. A spectral boundary integral method for flowing blood cells. *Journal of Computational Physics* 2010; **229**:3726–3744.
37. Wu J, Aidun CK. Simulating 3D deformable particle suspensions using lattice Boltzmann method with discrete external boundary force. *International Journal for Numerical Methods in Fluids* 2010; **62**:765–783.
38. Noguchi H. Swinging and synchronized rotations of red blood cells in simple shear flow. *Physical Review E* 2009; **80**:021902.
39. Sui Y, Chew YT, Roy P, Cheng YP, Low HT. Dynamic motion of red blood cells in simple shear flow. *Physics of Fluids* 2008; **20**:112106.
40. Fischer TM, Stöhr-Liesen M, Schmid-Schönbein H. The red cell as a fluid droplet: tank tread-like motion of the human erythrocyte membrane in shear flow. *Science* 1978; **202**:894–896.
41. Tran-Son-Tay R, Sutera SP, Rao PR. Determination of red blood cell membrane viscosity from rheoscopic observations of tank-treading motion. *Biophysical Journal* 1984; **46**:65–72.
42. Dintenfass L. Molecular rheology of human blood; Its role in health and disease (Today and Tomorrow). In *Proceedings of 8^{th} International Congress of Rheology (Naples)*, Vol. 3, Astarita G, Marrucci G, Nicilais L (eds). Springer: New York, 1980; 467–480.
43. Lowe GDO. *Clinical Blood Rheology*, Vol. I & II. CRC Press: Boca Raton, FL, 1998.
44. Robertson AM, Sequeira A, Kameneva MV. Hemodynamical flows. *Modeling, Analysis and Simulation (Oberwolfach Seminars, Birkhauser Verlag, Basel)* 2008; **37**:63–120.

DOI: 10.1002/fld